New Journal of Physics
The open access journal at the forefront of physics

Deutsche Physikalische Gesellschaft DPG
IOP Institute of Physics

Published in partnership with: Deutsche Physikalische Gesellschaft and the Institute of Physics

OPEN ACCESS

RECEIVED
29 October 2017

REVISED
25 February 2018

ACCEPTED FOR PUBLICATION
16 March 2018

PUBLISHED
20 April 2018

PAPER

High-energy coherent terahertz radiation emitted by wide-angle electron beams from a laser-wakefield accelerator

Xue Yang[1], **Enrico Brunetti**[2] **and Dino A Jaroszynski**[2,3]

[1] Department of Physics, Capital Normal University, Key Lab of Terahertz Optoelectronics, Ministry of Education, and Beijing Advanced Innovation Center for Imaging Technology, Beijing 100048, People's Republic of China
[2] SUPA, Department of Physics, University of Strathclyde, Glasgow, G4 0NG, United Kingdom
[3] Author to whom any correspondence should be addressed.

E-mail: d.a.jaroszynski@strath.ac.uk

Keywords: coherent transition radiation, terahertz generation, laser-wakefield acceleration

Abstract

High-charge electron beams produced by laser-wakefield accelerators are potentially novel, scalable sources of high-power terahertz radiation suitable for applications requiring high-intensity fields. When an intense laser pulse propagates in underdense plasma, it can generate femtosecond duration, self-injected picocoulomb electron bunches that accelerate on-axis to energies from 10s of MeV to several GeV, depending on laser intensity and plasma density. The process leading to the formation of the accelerating structure also generates non-injected, sub-picosecond duration, 1–2 MeV nanocoulomb electron beams emitted obliquely into a hollow cone around the laser propagation axis. These wide-angle beams are stable and depend weakly on laser and plasma parameters. Here we perform simulations to characterise the coherent transition radiation emitted by these beams if passed through a thin metal foil, or directly at the plasma–vacuum interface, showing that coherent terahertz radiation with 10s μJ to mJ-level energy can be produced with an optical to terahertz conversion efficiency up to 10^{-4}–10^{-3}.

1. Introduction

Terahertz (THz) radiation, which lies between mid-infrared and microwaves, is of great interest to researchers and industrialists because of the wide range of applications [1–7]. Several different mechanisms for generating electromagnetic fields within this so-called 'THz gap', between 0.1 and 10 THz, have been explored. Among these, acceleration of photocarriers in semiconductor antennas [8] and optical rectification in electro-optic crystals [9] are currently the most widely used. However, the relatively low damage threshold of optical materials restricts the maximum energies possible. Plasma, in contrast, has no such limitation as it is already broken down. Because of the high currents that it can sustain, it offers the potential of generating very intense THz radiation, which could be useful for applications investigating nonlinear processes [10, 11].

Laser–plasma interactions involve a rich range of physical processes that occur during and immediately after interaction, which include several mechanisms for the generation of THz radiation. For example, in recent years, moderate intensity lasers have been used to generate air–plasma filaments [12–14], in particular with two-colour laser fields [15–20]. This produces emission of conical THz radiation with conversion efficiencies as high as 10^{-3}, although saturation tends to occur at high laser intensities [18]. Laser–solid interactions at high intensities can produce THz radiation through several mechanisms, which typically involve the excitation of surface currents on solid targets [21–25], embedded plasma dipoles [26] and also coherent transition radiation (CTR) at boundaries and interfaces [27–29]. These methods can lead to high energies (in the sub-millijoule range) and high peak electric fields (1–100s MV cm^{-1}), which can be scaled with the laser intensity [24, 25]. However, a fresh target surface is required for each shot, multiple beams are sometimes necessary, and stability and debris are also challenging. In contrast, THz generation schemes based on laser–gas interactions employ gas nozzles where fresh plasma is produced on each shot. Another common scheme for generating THz radiation is

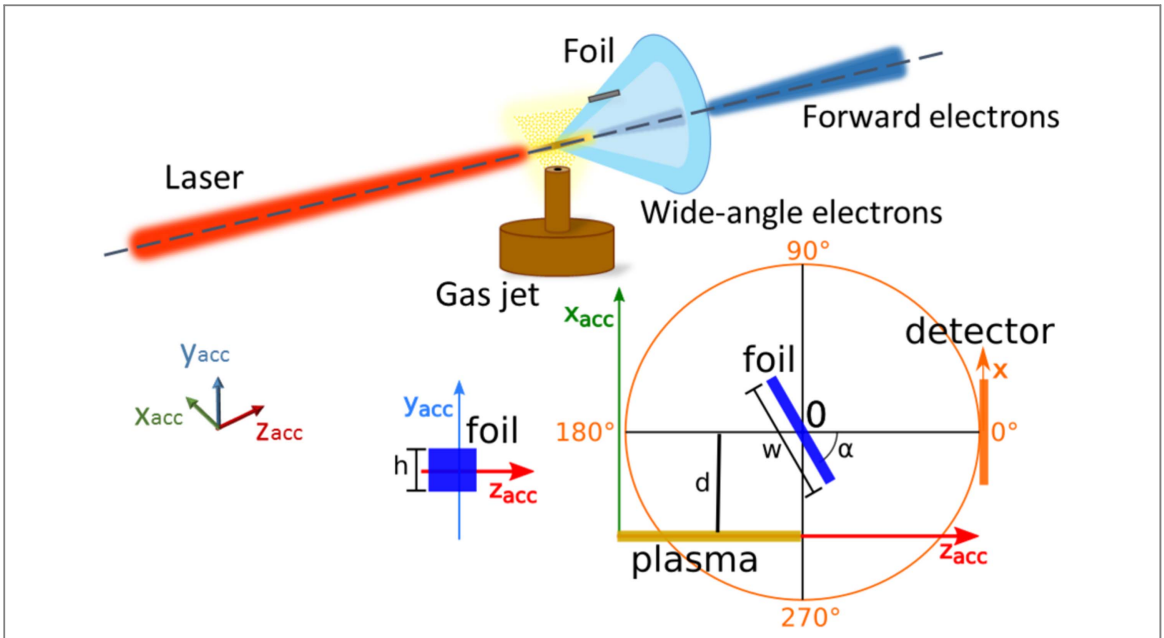

Figure 1. Schematic diagram of a THz source driven by wide-angle electron beams. An intense laser pulse focused onto a gas jet accelerates oblique electrons that generate CTR on a rectangular foil with width w and height h, offset by a distance d from the laser axis and oriented at an angle α perpendicular to the horizontal plane z_{acc}–x_{acc}.

the emission of CTR from electron beams crossing an interface between two media of different dielectric constant [30]. Leemans *et al* [31] reported the observation of THz radiation with energies of 3–5 μJ sr^{-1} when forward electron beams with 5 MeV energy, with a Maxwellian velocity-distribution and nC-level charge from a laser-wakefield accelerator (LWFA) cross the plasma–vacuum boundary. CTR with spectra extending from microwaves to the near infrared is also produced when high-energy electron beams from both conventional and LWFAs pass through a metallic foil [32–35]. This paper investigates the production of THz radiation from very high-charge, wide-angle electron beams from a LWFA that are not injected into the wake [36, 37]. We show that these obliquely emitted beams, with nC-level charge and 1–2 MeV energy, can produce 10s μJ to mJ-level THz radiation when passed through a foil or at the plasma–vacuum boundary of the accelerator.

2. Theoretical model

Figure 1 shows a schematic diagram of a THz radiation source based on wide-angle electron beams from a LWFA. An infrared laser pulse is focused to relativistic intensities ($I > 10^{18}$ W cm^{-2}) onto a gas target and emits a high-charge, low-energy electron beam in a wide forward cone around the laser propagation axis. High-energy electron bunches with typically 1%–10% energy spread can also be accelerated along the laser axis. The LWFA is modelled in three-dimensional geometry using the particle-in-cell (PIC) code Object-oriented Simulation Rapid Implementation System (OSIRIS) [38] and details of these simulations are presented in [36]. A selection of the phase-space distribution of wide-angle electrons obtained with OSIRIS is loaded into a code based on the vector model described in [39], which calculates transition radiation (TR) from a perfectly conducting screen of arbitrary shape and orientation for arbitrary electron energies and particle numbers. This screen can represent an inserted foil or the plasma–vacuum boundary. We now briefly review the physics of LWFAs and describe the model used to calculate TR. Simulation results are presented in the next section.

2.1. Laser-wakefield acceleration

The emission of wide-angle electron beams from a LWFA is driven by the same mechanism responsible for the generation of high-energy forward electron beams. The ponderomotive force of an intense laser pulse propagating in an underdense plasma expels electrons away from the high intensity region, forming an ion-filled 'bubble' trailing behind the pulse [40, 41]. Some background electrons can become trapped inside the bubble, where they are exposed to electric fields in excess of 100 GV m^{-1} and accelerate to high energies over short distances. Energies up to 4.2 GeV have been achieved over centimetre-scale lengths [42]. Most electrons, however, are not injected into the bubble, but stream around the bubble walls as a sheath, where they can experience accelerating fields of about 10–100 GV m^{-1} in both longitudinal and transverse direction. The acceleration length is typically 5–10 μm in the transverse direction, limited by the bubble size, and 10–20 μm in

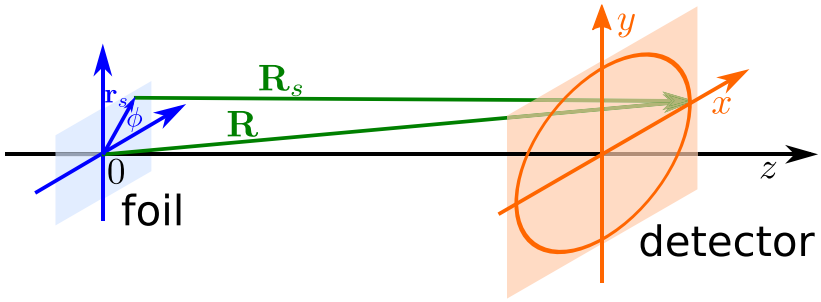

Figure 2. Schematic diagram used to calculate TR observed at **R** and emitted by an electron moving along z and crossing a conducting screen at the point **O**.

the laser propagation direction, since electrons can travel some distance with the bubble before being ejected. Some of these sheath electrons gain an energy of 1–2 MeV through a sling-shot action and exit the plasma at an angle of 30°–60° with respect to the laser propagation direction, depending on the specific energy gain. Often, electrons travelling near the bubble interior gain a higher momentum, especially in the longitudinal direction, and are expelled closer to the laser axis, whereas electrons travelling further away from the bubble interior gain lower energy and are ejected at a larger angle. These wide-angle electrons form a cone containing up to 10s-nC total charge in a bunch with duration of the order of 1 ps, based on PIC simulations. Experiments and simulations show that wide-angle beams are emitted with high stability and little variation in energy and ejection angle for a wide range of laser and plasma parameters [36, 37].

2.2. Transition radiation

When the field of a charged particle encounters an obstacle, such as a foil or dielectric plate, surface currents and charge densities are excited, causing the emission of transition or diffraction radiation. Several methods and approximations have been employed to calculate the energy distribution of TR for different geometries [43–46]. Here we follow the approach described in [39], where electromagnetic equivalence theorems are used to calculate TR from a perfectly conductive foil as the emission of a virtual magnetic surface current $\mathbf{j} = -\epsilon_0 c \mathbf{n_s} \times \mathbf{E_e}$, where $\mathbf{n_s}$ is the normal vector to the foil, $\mathbf{E_e}$ is the electron's field, ϵ_0 the vacuum permittivity and c the speed of light.

For the geometry illustrated schematically in figure 2, the vector potential describing TR is

$$\mathbf{A} = -\frac{1}{2\pi c}\int \mathbf{n_s} \times \mathbf{E_e}\frac{e^{ikR_s}}{R_s}\frac{\rho d\rho d\phi}{|n_{s,z}|},$$

where $R_s = |\mathbf{R} - \mathbf{r_s}|$ is the distance from the surface element $\mathbf{r_s}$ to the observation position $\mathbf{R}$ and $k = \omega/c$, with ω the radiation angular frequency and c the speed of light. In cylindrical coordinates (ρ, ϕ, z), the Fourier components of the electric field of an electron with charge $q = -e$ moving along z with velocity βc are

$$E_{e_\rho} = \frac{q}{(2\pi)^{3/2}\epsilon_0 c}\frac{k_e}{\beta\gamma}K_1\left(\frac{k_e}{\gamma}\rho\right)e^{ik_e z},$$

$$E_{e_z} = -i\frac{q}{(2\pi)^{3/2}\epsilon_0 c}\frac{k_e}{\beta\gamma^2}K_0\left(\frac{k_e}{\gamma}\rho\right)e^{ik_e z},$$

with $\gamma = 1/\sqrt{1-\beta^2}$ the Lorentz factor, K_n the nth modified Bessel function of the second kind, $k_e = k/\beta$ and ϵ_0 the vacuum permittivity. The field components in Cartesian coordinates are

$$E_{e_x} = E_0\frac{k}{\beta^2\gamma}K_1\left(\frac{k}{\beta\gamma}\rho\right)e^{ikz/\beta}\cos\phi,$$

$$E_{e_y} = E_0\frac{k}{\beta^2\gamma}K_1\left(\frac{k}{\beta\gamma}\rho\right)e^{ikz/\beta}\sin\phi,$$

$$E_{e_z} = -iE_0\frac{k}{\beta^2\gamma^2}K_0\left(\frac{k}{\beta\gamma}\rho\right)e^{ikz/\beta},$$

with $E_0 = \frac{q}{(2\pi)^{3/2}\epsilon_0 c}$. After defining $\tilde{\mathbf{j}} = -\frac{\mathbf{j}}{\epsilon_0 c} = \mathbf{n_s} \times \mathbf{E_e}$, one finds that

$$\tilde{\mathbf{j}} = (\tilde{j}_x, \tilde{j}_y, \tilde{j}_z) = (n_y E_{ez} - n_z E_{ey}, n_z E_{ex} - n_x E_{ez}, n_x E_{ey} - n_y E_{ex})$$

and

$$\tilde{j}_x = E_0 \frac{k}{\beta^2\gamma}\left[-\sin\phi K_1\left(\frac{k}{\beta\gamma}\rho\right)n_z - \frac{\mathrm{i}}{\gamma}K_0\left(\frac{k}{\beta\gamma}\rho\right)n_y\right]\mathrm{e}^{\mathrm{i}kz/\beta},$$

$$\tilde{j}_y = E_0 \frac{k}{\beta^2\gamma}\left[\cos\phi K_1\left(\frac{k}{\beta\gamma}\rho\right)n_z + \frac{\mathrm{i}}{\gamma}K_0\left(\frac{k}{\beta\gamma}\rho\right)n_x\right]\mathrm{e}^{\mathrm{i}kz/\beta},$$

$$\tilde{j}_z = E_0 \frac{k}{\beta^2\gamma}\left[\sin\phi K_1\left(\frac{k}{\beta\gamma}\rho\right)n_x - \cos\phi K_1\left(\frac{k}{\beta\gamma}\rho\right)n_y\right]\mathrm{e}^{\mathrm{i}kz/\beta}.$$

The electric and magnetic fields are

$$\mathbf{E} = -\mathrm{i}c\,\mathbf{k}\times\mathbf{A}, \qquad \mathbf{B} = \frac{1}{ck}\mathbf{k}\times\mathbf{E},$$

where the second equation is exact, whereas the first equation is valid at a distance from the source sufficiently large to allow for the radiation's wavefront to be almost spherical (quasi-spherical approximation). This condition is less restrictive than the far-field approximation, which requires an observation distance $R \gg \gamma^2\lambda$, with λ the radiation wavelength [39]. Often the calculation of CTR emitted by ultra-relativistic particles is further simplified by neglecting the longitudinal component E_{e_z} of the electron's field (scalar approximation) and the foil orientation. However, for the low energies and large incidence angles encountered here, these approximations are not valid and the more accurate vector model is used. The energy radiated per unit frequency interval and per unit area is derived from the Poynting vector, obtaining [44]

$$\frac{\mathrm{d}U}{\mathrm{d}\omega\mathrm{d}x\mathrm{d}y} = 2\epsilon_0 c|\mathbf{E}(\omega,\,\mathbf{R})|^2.$$

Transition radiation is calculated numerically for each electron in a coordinate system that is translated and rotated to align the direction of motion with the z-axis. The electric field produced by each electron at the observation point is summed to obtain the full beam emission and the corresponding energy density. A space-frequency grid is employed to calculate the energy density at different positions and frequencies, and numerical integrations are performed to obtain the radiation spectrum and total energy. Most results presented here are obtained using 20 000 electrons and rescaled to higher beam charges using the quadratic dependence reported in section 3. The foil-detector distance is 500 mm, comparable to the likely scale of experiments. Often, large source-detector distances are required for long wavelength radiation to become fully formed. However, for the low electron energies considered here, the formation length is of the order of millimetres, as discussed below.

2.3. Single-particle TR

In order to facilitate the interpretation of the simulation results presented in the next section for wide-angle electron beams, we describe here the angular properties of TR emitted by a single electron, using the vector model introduced previously. Figure 3 shows horizontal scans of the energy density of TR generated by an electron with different energies moving in the 0° direction and passing through the centre of a 3 mm × 3 mm foil oriented at different angles. Plots on the right column correspond to an electron energy of 10 MeV and reproduce the characteristic TR pattern, with forward emission in a narrow hollow cone peaked at an angle $1/\gamma$ with respect to the electron path direction, and backward radiation produced in the specular direction. When the electron crosses the foil at normal incidence (top row) the four radiation lobes are symmetric, whereas for oblique incidence the lobes closer to the surface are more intense. This asymmetry is due to the longitudinal component of the electron's field [47], and is stronger at low energies and large incidence angles, almost vanishing for energies beyond approximately 50 MeV. For 10° orientation (bottom row), most radiation is emitted in direction almost parallel to the foil surface and some of the lobes are not clearly distinguishable.

TR produced by a beam with non-zero energy spread and divergence can be considered as the convolution of the signal emitted by a single electron with the distribution function representing the bunch shape. Typically this results in the broadening of the forward and backward cones, which can become partially filled also for highly relativistic beams. In the case of wide-angle electron beams, the bunch shape is complex and evolves quickly, therefore numerical simulation are required.

3. Simulation results

We now present simulation results of CTR produced by wide-angle electron beams as they cross a conducting surface with varying size, position and orientation, modelling the emission of CTR at both the plasma–vacuum boundary and from inserted foils. We show that 10s μJ to mJ-level coherent radiation is produced in the spectral region between 0.1 and 5 THz, peaked at a frequency that depends on the size and location of the foil.

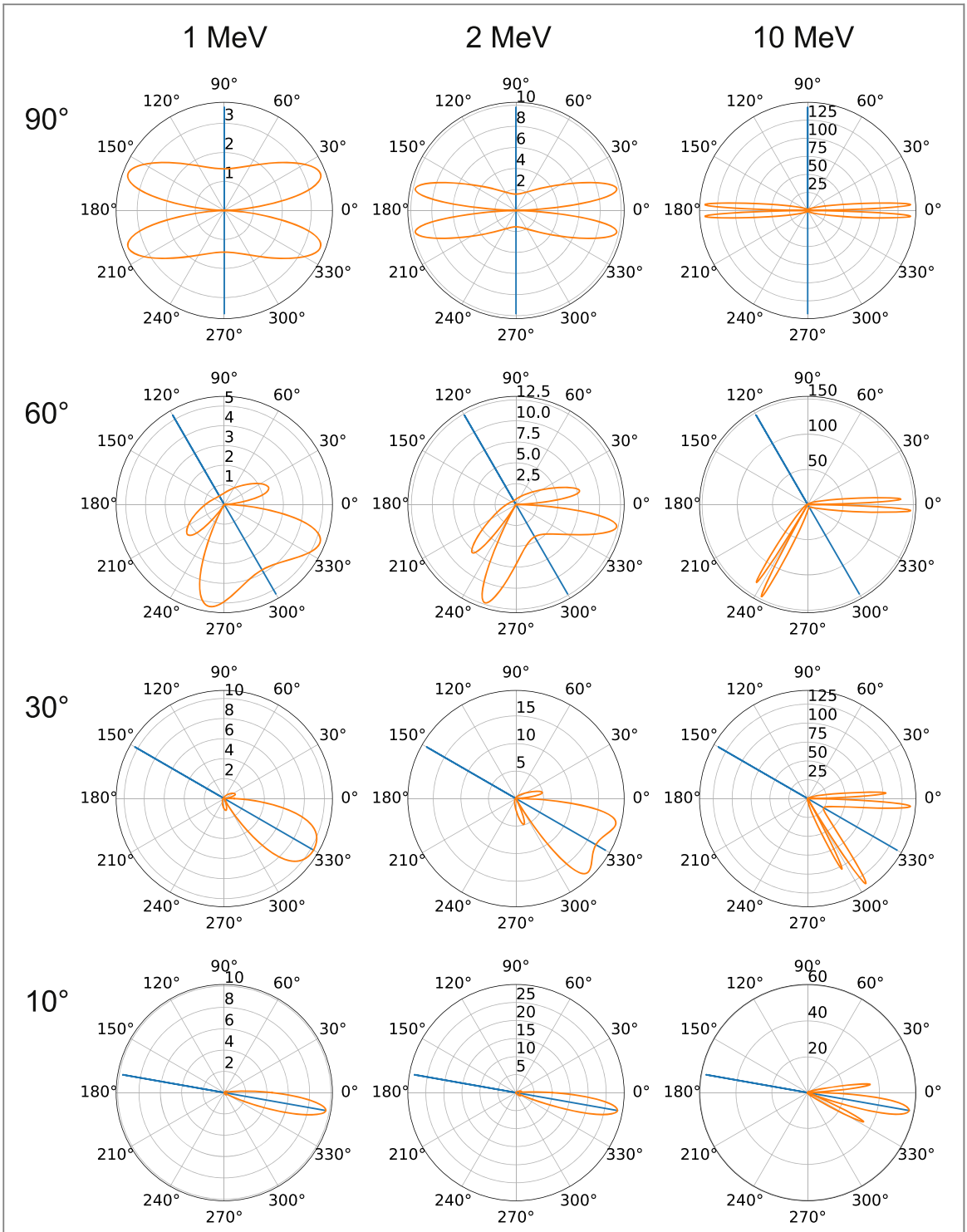

Figure 3. Energy density (10^{-24} J sr^{-1}) integrated between 0.3 and 4 THz of TR emitted by a single electron with 1 (left column), 2 (middle column) and 10 (right column) MeV energy from a 3 × 3 mm foil with 90° (top row), 60° (second row) 30° (third row) and 10° (bottom row) orientation. The observation point is at a distance of 500 mm from the foil in the x–z plane. The thick blue line shows the foil orientation.

The properties of oblique electron beams have been studied for a wide range of laser and plasma parameters, finding little variation in the angular distribution and energy spectrum, whereas the charge scales linearly with laser intensity and plasma density. Therefore, the angular distribution and spectrum of CTR also change little. As a representative example, we show results obtained for parameters similar to the experiments on the characterisation of wide-angle electron beams reported in [36]. A horizontally polarized laser with 0.8 μm wavelength, normalized vector potential $a_0 = 3$, spot radius $w_0 = 7$ μm and 20 fs pulse duration interacts with a pre-ionized plasma with density 2×10^{19} cm^{-3} and 500 μm length. A wide-angle electron beam is emitted in a cone with 38° ± 13° aperture angle from the laser axis. The energy distribution is exponential, with a mean of

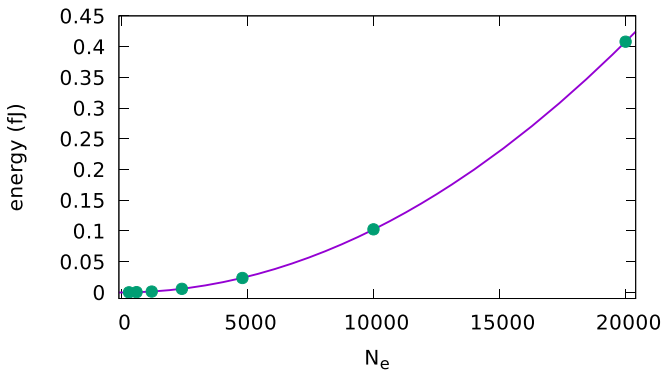

Figure 4. Energy versus number of simulation particles for CTR emitted by a 1 mm × 1 mm foil with 60° orientation and 100 μm offset, integrated between 0.3 and 4 THz and between −500 and 500 mm in x and y.

1.8 MeV (Lorentz factor $\gamma = 4.5$), and the total charge in the full cone is 10 nC. Electrons in the left section of the cone ($x_{acc} > 0$) with energy greater than 0.5 MeV are ballistically propagated to a rectangular surface perpendicular to the z_{acc}–x_{acc} plane, placed at varying offsets and angles from the laser axis (see insert in figure 1). For the chosen surface position, the electron beam passes close to the centre. Similar results are expected for the other sections of the cone, although the charge density can be smaller in the vertical axis, perpendicular to the laser polarization direction. Scattering in the foil has been simulated using Geant4 [48] and its effect is found to be small, since the electron beam divergence is already large. The energy loss is also small for foils with thickness of a few hundreds μm or less. These effects are neglected in the results presented here.

The scaling of TR power with electron beam charge has been verified by performing a simulation using a varying number of particles. As shown in figure 4, the radiation energy scales as the square of the number of electrons, indicating a high degree of coherence. Results presented here use a portion of the electron beam cone and assume a charge of 1 nC, matching the experimental results of [36] and the predictions of PIC simulations for similar laser parameters. The radiation yield for different beam charges can be estimated using this quadratic dependence, at least for comparable electron energy and spatial distributions.

3.1. Effect of foil orientation

Figure 5 shows a horizontal scan of the energy density of CTR generated by wide-angle electrons passing through a 1 mm × 0.5 mm foil offset by 100 μm from the laser axis for different orientations. As shown in section 2.3, highly relativistic electron bunches emit CTR in a narrow hollow cone peaked at an angle $1/\gamma$ with respect to the electron path direction. Backward radiation is also produced in the specular direction in a hollow cone with orientation that depends on the particle incidence angle on the foil. Because of the low energy and large divergence of wide-angle electron beams, the results obtained here are characterized by a broad and asymmetric angular distribution. For a foil parallel to the laser axis (figure 5(a)), the electron mean incidence angle is about 55° from normal (35° from the beam axis), similar to the third row in figure 3, where the incidence angle is 30° from the beam axis. CTR is emitted mostly in the direction parallel to the foil, peaked at an angle of about 10°. As the foil is rotated, the angular distribution becomes more symmetric and the forward and backward lobes become gradually distinguishable.

The spatial, spectral and temporal profile of one of these lobes is shown in figure 6 for the case of 60° orientation (figure 5(c)) and observation plane centred at 0°, perpendicular to the z–x plane (see insert in figure 1). The FWHM divergence is 39° in the horizontal direction and 44° in the vertical direction, with spectrum peaked at 0.6 THz and total energy of 45 μJ, assuming a 1 nC electron beam charge. The energy of the driving laser is about 300 mJ and the optical to terahertz efficiency is about 1.5×10^{-4}. The energy contained in the electron beam is 1.8 mJ for 1 nC charge and the conversion efficiency from electrons to CTR is about 2.5×10^{-2}. Transition radiation is emitted over a large angle due to the low electron beam energy and this large divergence may not be ideal for some applications. However, it is possible to re-collimate or focus the CTR beam close to the source, for example using an off-axis parabola with a hole, because for such low electron energies the formation length is short. For forward emission at wavelength λ and angle θ, it is $z_f = \beta\lambda/[2\pi(1 - \beta\cos\theta)]$, with β the electron velocity over the speed of light. The electron beam path should be unobstructed for distances longer than the formation length in order to prevent attenuation of the emitted radiation [49, 50]. For 2 MeV energy, $\theta = 1/\gamma$ and 0.5 THz frequency, $z_f \approx 2$ mm. In contrast, $z_f \approx 8$ m for a 150 MeV electron beam, which makes it difficult to perform experiments with a fully formed beam in a compact space.

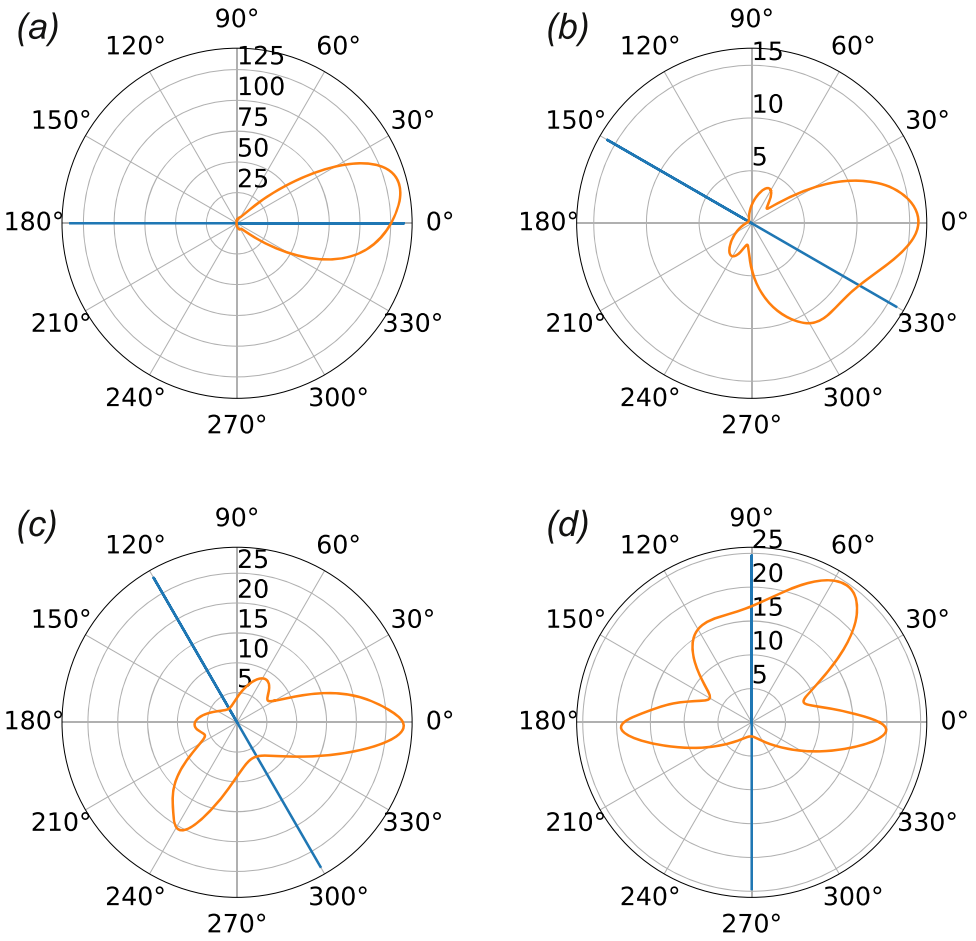

Figure 5. Energy density (μJ sr^{-1}) integrated between 0.3 and 4 THz of CTR by a 1 $\times$ 0.5 mm foil offset by 100 μm from the laser axis and with (a) parallel ($\alpha = 0°$), (b) 30°, (c) 60° and (d) 90° orientation. The observation point is at a distance of 500 mm from the foil in the x–z plane. The thick blue line shows the foil orientation.

A PIC simulation performed for higher laser energy ($a_0 = 8$), while keeping the same plasma parameters and laser spot size, predicts an increase of the electron beam charge by a factor of 6 and a mean energy of 2.5 MeV. The CTR radiation obtained using this new phase-space distribution for the same geometry of figure 6 is still peaked at 0.6 THz and has the same divergence, with an energy of 1.5 mJ for a 6 nC electron beam charge, indicating that most of the electrons radiate coherently. In this case the energy of the driving laser is about 2.3 J, and the optical to terahertz efficiency is about 5 $\times$ 10^{-4}, which could be increased to 10^{-3} by using a larger fraction of the wide-angle electron beam. The energy contained in the electron beam is 15 mJ for 6 nC charge and the conversion efficiency from electrons to CTR is about 0.1.

3.2. Effect of foil size

The PIC simulations performed here use a uniform pre-ionised plasma with radius of approximately 20 μm, reproducing conditions typically found in LWFAs based on gas jets, where the driving laser pulse creates a long plasma channel with transverse radius typically between 10 and 30 μm, depending on laser and target parameters. We now present results of CTR produced on a surface parallel to the laser propagation axis, with 22 μm transverse offset, which is indicative of the emission expected at the plasma–vacuum boundary. Simulations performed for 30 μm offset produce almost identical results, suggesting that small variations in the transverse size of the plasma do no cause significant changes. On the other hand, the CTR spectrum and yield of simulations performed with an offset of several 100s μm is significantly different, because of the rapid evolution of the electron beam, as discussed below.

The dependence of the CTR spectrum on the radiator size is shown in figure 7 for a rectangular foil parallel to the laser axis, with a 22 μm offset, 1 mm width and varying height. The radiation is spatially integrated over a 500 mm $\times$ 500 mm detection area and the electron beam charge is fixed at 1 nC. As the foil height decreases, the CTR signal becomes weaker and the peak shifts towards higher frequencies, because the low-frequency side of the spectrum is suppressed when the radiator is smaller than the effective CTR source size $\gamma\lambda$, which is 1 mm for $\nu = 1$ THz and $\gamma \approx 3.5$ [51]. In a LWFA, the plasma is long and narrow, therefore the spatial distribution of

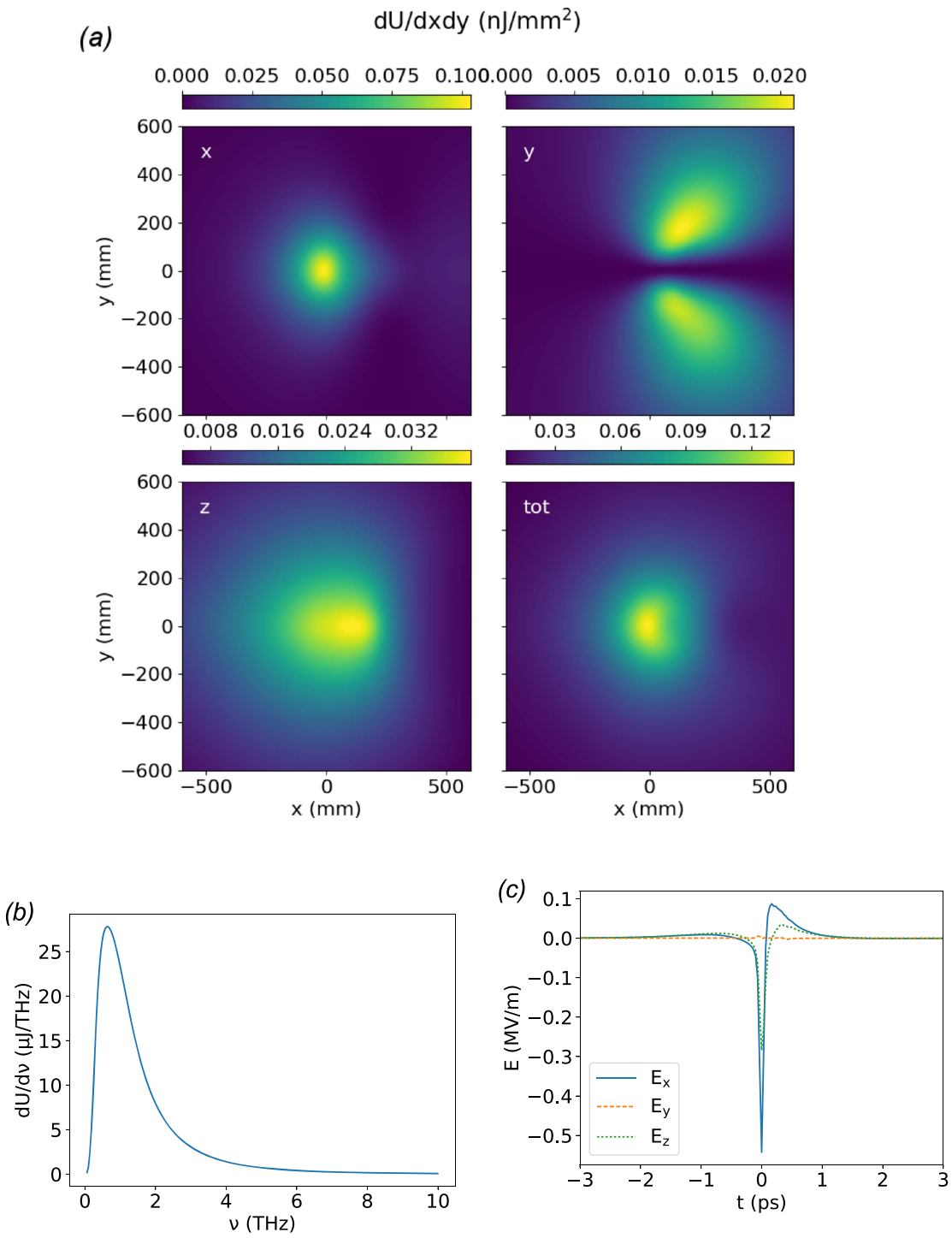

Figure 6. (a) Spatial, (b) spectral and (c) temporal profile of CTR emitted at 0° for the same parameters of figure 5(c). The four plots in figure (a) correspond to the frequency-integrated energy density contained in the three components of the electric field E_x, E_y, E_z and to the total energy density.

wide-angle electron beams is elongated along the laser propagation direction. The foil height can be changed without losing a large amount of charge, enabling a way to tune the spectrum. In particular, the curve for 20 μm is also representative of the CTR emission expected from wide-angle electron beams as they cross the vacuum–plasma boundary, which presents a sharp transition, comparable to the boundary between vacuum and a perfect conductor [52]. The angular distribution of CTR generated under these conditions is similar to the results of figure 5(a), with emission mostly parallel to the laser axis. This radiation can be collected and focused using an off-axis parabola with a hole in the centre to let the laser beam and the high-energy forward electron bunches through.

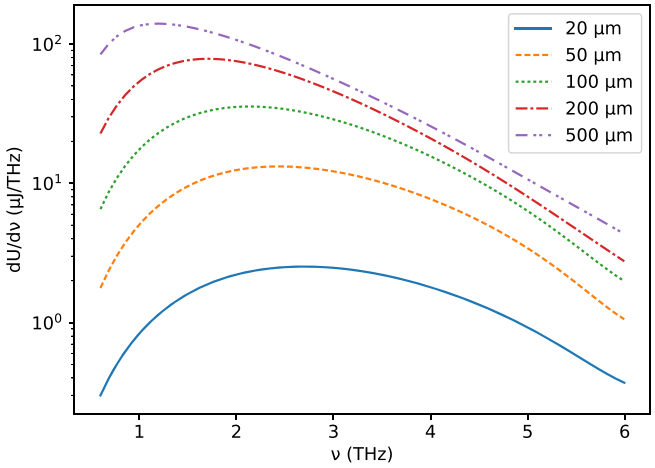

Figure 7. Spectrum of CTR produced by a 1 mm wide foil with varying height at an offset of 22 μm from the laser axis and parallel orientation.

3.3. Effect of foil position

A fundamental difference between high-energy forward electron beams from a LWFA and wide-angle beams is the bunch length. The longitudinal diameter of the bubble structure driving LWFAs is about 10–30 μm, depending on laser and plasma parameters [41]. Electrons injected into the bubble typically occupy a small fraction of this size and the electron bunch duration is about 1–10 fs [34, 35]. CTR produced by such short bunches has a broad spectrum, extending from THz frequencies or longer to the near infrared. Wide-angle electron beams, on the other hand, are continuously ejected over at least 100s μm propagation distances behind the driving laser and the bunch duration has ps-scale, based on PIC simulations. As they leave the plasma, both the bunch length and beam size increase further, causing the suppression of the high-frequency side of the spectrum.

In general, the total power P of TR is the sum of the contribution P_0 from each electron, according to the formula $P = [N_e + N_e^2 f(\mathbf{x}, \nu, \alpha)]P_0$, where N_e is the number of electrons and f is the bunch form factor, which is a function of the electron spatial distribution, radiation frequency ν and foil orientation α. If the transverse beam size is smaller than the longitudinal length σ_L, then $f \approx 1$ for $\lambda \gg \sigma_L$ and emission at these wavelengths is coherent, with the power growing quadratically with the number of particles. For example, a 1 ps ($\sigma_L \approx 300$ μm) bunch length corresponds to coherent emission at frequencies lower than about 1 THz. If the transverse beam size is large, radiation emitted by electrons at different positions on the foil is no longer in phase, resulting in further suppression of the high frequencies. The phase-space distributions produced by PIC simulations show that in the case of wide-angle electron beams, the bunch duration, defined as the FWHM in direction of the foil normal, typically grows from about 300–500 fs at the accelerator exit to 1–2 ps at a distance of 1 mm from the laser axis, depending on foil size and orientation. The transverse beam size, defined as the FWHM in the horizontal and vertical directions on the foil plane, grows from about 0.2 mm $\times$ 0.05 mm to 1 mm $\times$ 0.5 mm over the same distance. This results in a shift of the high-frequency cut-off to about 0.5 THz. Wide-angle electron beams, however, have a complex three-dimensional distribution that cannot be separated into longitudinal and transverse components, making the definition of bunch length and transverse beam size somewhat arbitrary. An accurate prediction of the properties of CTR requires simulations where the fields generated by many electrons are summed numerically, as performed here. Examples are given in figure 8 for CTR emitted from a 3 mm $\times$ 3 mm foil with parallel orientation to the laser axis, showing that the spectrum shifts towards lower frequencies as the electron beam leaves the plasma. Here a larger foil size is used to avoid the suppression of the low-frequencies described above, as well as to intercept a larger fraction of the electron beam. Results depend weakly on the foil orientation. For example, an angle of 60° results in a shift by about 0.15 THz towards higher frequencies in the case of 1000 μm offset.

4. Conclusions

We have shown, using numerical simulations, that wide-angle electron beams produced by LWFAs can deliver 10s μJ to mJ-level, single-cycle radiation in the 0.1–5 THz spectral region, depending on the radiator size and location. At the vacuum–plasma boundary, the spectrum of CTR is peaked at about 2–3 THz, with the low frequency part suppressed because of the small transverse size of the radiator, which is typically about

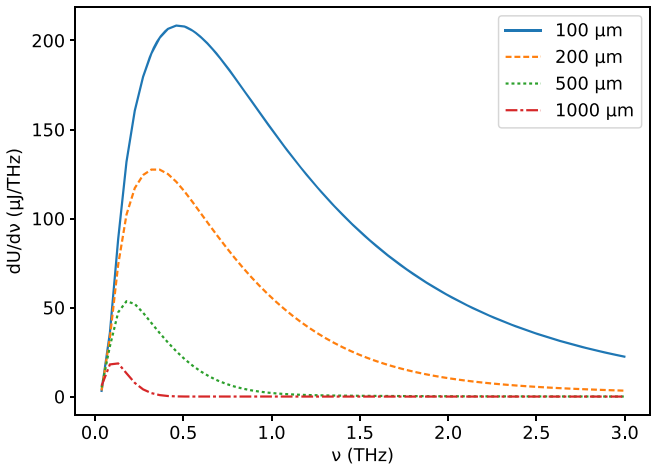

Figure 8. Spectrum of CTR produced on a 3 mm × 3 mm foil with parallel orientation to the laser axis and varying offset.

20–30 μm. As the electron beam leaves the plasma, the longitudinal and transverse size increase quickly and a foil inserted at a distance of about 0.1–1 mm from the accelerator exit would produce CTR with spectrum shifted to approximately 0.1–1 THz.

Experimental and theoretical studies of wide-angle electrons indicate that THz radiation should be emitted with high reproducibility on every laser shot. Radiation from the plasma–vacuum boundary could be collected using an off-axis parabola with a hole, to let the laser and high-energy electron beam through. Radiation from an inserted screen could be produced by using a foil with a hole, utilising the full wide-angle beam. Alternatively, a foil or metallic tape could be placed off-axis. If required, a LWFA can be tuned to produce only wide-angle beams, with no emission of high-energy femtosecond forward electron bunches. We observed experimentally that this can be achieved, for example, by decreasing the laser energy or by focusing the laser pulse at different positions in the gas target, along the longitudinal axis.

It was also found that the charge of wide-angle electron beams increases linearly with laser intensity and plasma density [36, 37]. Therefore, the energy of THz radiation can also scale to mJ-levels, which would make an intense source of THz radiation with peak powers in excess of GW peak powers, comparable with a far-infrared free-electron laser (FEL) [53]. For current 10 Hz, 10s TW lasers, an average power of 10–100 mW is expected over the far-infrared spectral range. Future 1 kHz lasers would extend the average power to 1 W, which is comparable with a far-infrared FEL. This source of THz radiation based on underdense plasma has advantages over comparable THz sources based on laser–solid interactions. Further research is required to experimentally characterize these pulses and fully explore the potential of LWFAs for the production of intense THz radiation.

Acknowledgments

The authors thank the OSIRIS consortium (UCLA/IST) for the use of OSIRIS. Computational results were obtained using ARCHIE-WeSt (EPSRC EP/K000586/1). The authors acknowledge funding from UK EPSRC (EP/J018171/1, EP/N028694/1), EU H2020 Research and Innovation Programme LASERLAB EUROPE (654148) and EuPRAXIA (653782). Data associated with research published in this paper is available at http://doi.org/10.15129/2d34924e-b2f0-4c75-b36b-8abb13cbdf55.

References

[1] Tonouchi M 2007 *Nat. Photon.* **1** 97–105
[2] Jepsen P, Cooke D and Koch M 2011 *Laser Photonics Rev.* **5** 124–66
[3] Shen Y C 2011 *Int. J. Pharm.* **417** 48–60
[4] Son J H 2013 *Nanotechnology* **24** 214001
[5] Akyildiz I F, Jornet J M and Han C 2014 *Phys. Commun.* **12** 16–32
[6] Stecher M, Jördens C, Krumbholz N, Jansen C, Scheller M, Wilk R, Peters O, Scherger B, Ewers B and Koch M 2016 Towards industrial inspection with THz systems *Ultrashort Pulse Laser Technology* (*Springer Series in Optical Sciences* vol 195) (Cham: Springer) pp 311–35
[7] Dhillon S S *et al* 2017 *J. Phys. D: Appl. Phys.* **50** 043001
[8] Weling A S, Hu B B, Froberg N M and Auston D H 1994 *Appl. Phys. Lett.* **64** 137–9
[9] Zhang X C, Hu B B, Darrow J T and Auston D H 1990 *Appl. Phys. Lett.* **56** 1011–3
[10] Hafez H A, Chai X, Ibrahim A, Mondal S, Férachou D, Ropagnol X and Ozaki T 2016 *J. Opt.* **18** 093004
[11] Zhang X C, Shkurinov A and Zhang Y 2017 *Nat. Photon.* **11** 16

[12] Sprangle P, Peñano J R, Hafizi B and Kapetanakos C A 2004 *Phys. Rev.* E **69** 066415
[13] Xie X, Dai J and Zhang X C 2006 *Phys. Rev. Lett.* **96** 075005
[14] D'Amico C, Houard A, Franco M, Prade B, Mysyrowicz A, Couairon A and Tikhonchuk V T 2007 *Phys. Rev. Lett.* **98** 235002
[15] Cook D J and Hochstrasser R M 2000 *Opt. Lett.* **25** 1210–2
[16] Kress M, Löffler T, Eden S, Thomson M and Roskos H 2004 *Opt. Lett.* **29** 1120–2
[17] Bartel T, Gaal P, Reimann K, Woerner M and Elsaesser T 2005 *Opt. Lett.* **30** 2805–7
[18] Kim K Y, Taylor A J, Glownia J H and Rodriguez G 2008 *Nat. Photon.* **2** 605
[19] Thomson M, Blank V and Roskos H 2010 *Opt. Express* **18** 23173–82
[20] Clerici M *et al* 2013 *Phys. Rev. Lett.* **110** 253901
[21] Hamster H, Sullivan A, Gordon S, White W and Falcone R W 1993 *Phys. Rev. Lett.* **71** 2725–8
[22] Sheng Z, Mima K, Zhang J and Sanuki H 2005 *Phys. Rev. Lett.* **94** 095003
[23] Sagisaka A *et al* 2008 *Appl. Phys.* B **90** 373–7
[24] Li Y T *et al* 2012 *Appl. Phys. Lett.* **100** 254101
[25] Gopal A, Singh P, Herzer S, Reinhard A, Schmidt A, Dillner U, May T, Meyer H G, Ziegler W and Paulus G G 2013 *Opt. Lett.* **38** 4705–7
[26] Kwon K B, Kang T, Song H S, Kim Y K, Hur M S, Ersfeld B and Jaroszynski D A 2018 *Sci. Rep.* **8** 145
[27] Liao G Q *et al* 2016 *Phys. Rev. Lett.* **116** 205003
[28] Ding W J and Sheng Z M 2016 *Phys. Rev.* E **93** 063204
[29] Mondal S *et al* 2017 *Sci. Rep.* **7** 40058
[30] Ginzburg V L 1982 *Phys. Scr.* **2** 182–91
[31] Leemans W *et al* 2003 *Phys. Rev. Lett.* **91** 074802
[32] Carr G L, Martin M C, McKinney W R, AU Jordan K, Neil G R and Williams G P 2002 *Nature* **420** 153–6
[33] Casalbuoni S, Schmidt B, Schmüser P, Arsov V and Wesch S 2009 *Phys. Rev. Spec. Top. Accel. Beams* **12** 030705
[34] Lundh O *et al* 2011 *Nat. Phys.* **7** 1745–2473
[35] Islam M R *et al* 2015 *New J. Phys.* **17** 093033
[36] Yang X *et al* 2017 *Sci. Rep.* **7** 43910
[37] Brunetti E *et al* 2017 *Proc. SPIE* **10240** 102400P
[38] Fonseca R A *et al* 2002 Osiris: a three-dimensional, fully relativistic particle in cell code for modeling plasma based accelerators *Computational Science-ICCS 2002, Pt III, Proc.* vol 2331, pp 342–51
[39] Shkvarunets A G and Fiorito R B 2008 *Phys. Rev. Spec. Top. Accel. Beams* **11** 012801
[40] Pukhov A and Meyer-ter-Vehn J 2002 *Appl. Phys.* B **74** 355–61
[41] Lu W *et al* 2007 *Phys. Rev. ST Accel. Beams* **10** 061301
[42] Leemans W P *et al* 2014 *Phys. Rev. Lett.* **113** 245002
[43] Verzilov V 2000 *Phys. Lett.* A **273** 135–40
[44] Casalbuoni S, Schmidt B and Schmüser P 2005 *Far-Infrared Transition and Diffraction Radiation Part I: Production, Diffraction Effects and Optical Propagation* TESLA-Report 2005-15 DESY
[45] Sütterlin D, Erni D, Dehler M, Jäckel H, Sigg H and Schlott V 2007 *Nucl. Instrum. Methods Phys. Res.* B **264** 361–70
[46] Karlovets D V and Potylitsyn A P 2008 *J. Exp. Theor. Phys.* **106** 1045
[47] Karlovets D and Potylitsyn A 2008 *Nucl. Instrum. Methods Phys. Res.* B **266** 3738–43
[48] Agostinelli S *et al* 2003 *Nucl. Instrum. Methods* **506** 250–303
[49] Shibata Y *et al* 1994 *Phys. Rev.* E **49** 785–93
[50] Baier V and Katkov V 2005 *Phys. Rep.* **409** 261–359
[51] Castellano M, Cianchi A, Orlandi G and Verzilov V A 1999 *Nucl. Instrum. Meth.* A **435** 297–307
[52] Schroeder C B, Esarey E, van Tilborg J and Leemans W P 2004 *Phys. Rev.* E **69** 016501
[53] Gensch M Super-radiant LINAC-based THz sources *Proc. FEL2013*